RSC Advances

PAPER

View Article Online
View Journal | View Issue

Cite this: *RSC Adv.*, 2026, **16**, 27655

Cryogenic magnetocaloric effect in a disordered double-perovskite Gd_2MnZnO_6

Dimitar N. Petrov,[a] J. Ćwik,[b] Yu. S. Koshkid'ko,[b] M. Babij,[b] T. A. Ho,[c] T. L. Phan,*[c] D. T. Khan,[d] N. T. Dang,[ef] K. T. H. My[g] and D.-H. Kim*[g]

This work presents an investigation on the structural characterization, magnetic behavior, and cryogenic magnetocaloric (MC) effect of a disordered double-perovskite Gd_2MnZnO_6 prepared *via* a solid-state reaction method. Powder X-ray diffraction analysis reflects that the title compound crystallizes in an orthorhombic structure with the *Pnma* space group. Its MC performance has been systematically assessed by means of the magnetic entropy change ($|\Delta S_m|$), adiabatic temperature change (ΔT_{ad}) and heat capacity C_p. As a result, under an applied field of 40 kOe, the directly measured ΔT_{ad} reaches approximately 2.6 K. Meanwhile, the largest $|\Delta S_m|$ and relative-cooling power values (RCP) are about 19 J kg^{-1} K^{-1} and 331 J kg^{-1}, respectively, for a magnetic-field change of 90 kOe. Such large values of the parameters characteristic for the MC effect make Gd_2MnZnO_6 a promising candidate for cryogenic magnetic refrigeration. Furthermore, analysis of the $M(T, H)$ and $|\Delta S_m(T)|$ data around the magnetic-phase transition indicates the presence of short-range magnetic order. This behavior is attributed to the coexistence of competing ferromagnetic and antiferromagnetic interactions in Gd_2MnZnO_6.

Received 29th March 2026
Accepted 14th May 2026

DOI: 10.1039/d6ra02602h

rsc.li/rsc-advances

1. Introduction

Magnetic cooling based on the magnetocaloric (MC) effect represents an attractive, energy-efficient alternative to conventional gas-compression refrigeration technology for both cryogenic and near-room-temperature applications. The MC effect is quantified most often by the isothermal magnetic entropy change ($|\Delta S_m|$), adiabatic temperature change (ΔT_{ad}), and relative cooling power (RCP) or refrigerant capacity (RC) for a given magnetic-field change (ΔH).[1] Lanthanide-containing oxides, and particularly Gd^{3+}-bearing compounds, are among the top MC-effect performers because the half-filled 4f subshell of Gd^{3+} produces a large, nearly isotropic magnetic moment ($\mu_{eff}{}^{Gd^{3+}} = 7.94$) due to zero orbital angular momentum ($L = 0$) that can be efficiently magnetized by an applied magnetic field.[2,3] This fact makes Gd-rich oxides highly promising for cryogenic refrigeration, where large entropy extraction per unit mass at low temperatures is required.

Double-perovskite oxides typically follow the general formula $Ln_2BB'O_6$ (Ln – lanthanide element, B/B′ – transition or main-group cations) and provide a chemically flexible framework for engineering magnetic interactions between 3d and 4f sublattices. In the family of Gd-containing double perovskites, two qualitatively different magnetic scenarios appear repeatedly in the literature and lead to fundamentally different MC behavior.[4–6] First, when the B/B′ sites contain magnetic 3d ions (like Ni, Co, and Mn arranged in an ordered rock-salt structure), double-exchange among 3d moments produces a transition to long-range ferromagnetic (FM) order at moderate temperatures.[7] The 3d sublattice ordering interacts with the large Gd^{3+} moments thus producing a large $|\Delta S_m|$ value near the 3d-ordering temperature and additional low-temperature contributions when the Gd sublattice is magnetized. Representative examples are Gd_2NiMnO_6 and Gd_2CoMnO_6, which show FM ordering at temperatures below the Curie temperature (T_C) of about 130 and 112 K, respectively, and a large cryogenic MC effect: Gd_2NiMnO_6 reaches $|\Delta S_m| = 35.5$ J kg^{-1} K^{-1} ($\Delta H = 70$ kOe) with $\Delta T_{ad} = 10.5$ K, while the polycrystalline Gd_2CoMnO_6 shows smaller values of $|\Delta S_m| = 24$ J kg^{-1} K^{-1} at $\Delta H = 70$ kOe.[8] These materials are notable because they combine a high $|\Delta S_m|$ and an insulating/low-loss character that is attractive for refrigeration applications at liquid-He and liquid-H_2 temperature ranges. It is also shown that Gd_2CoMnO_6 single crystal exhibits large anisotropic and rotational MC effect (MCE) due to Co–Mn sublattice anisotropy which changes the magnetization

[a]*Department of Physical Chemistry, Plovdiv University "Paisii Hilendarski", 24, Tsar Asen Str., 4000 Plovdiv, Bulgaria*

[b]*Institute of Low Temperature and Structure Research, PAS, Okólna 2, 50-422 Wroclaw, Poland*

[c]*Faculty of Physics Engineering and Nanotechnology, VNU University of Engineering and Technology, Vietnam National University, 144 Xuan Thuy Road, Cau Giay, Hanoi 100000, Vietnam. E-mail: ptlong2512@vnu.edu.vn*

[d]*University of Science and Education, The University of Danang, 550000 Danang, Vietnam*

[e]*Institute of Research and Development, Duy Tan University, 550000 Danang, Vietnam*

[f]*Faculty of Natural Sciences, Duy Tan University, 550000 Danang, Vietnam*

[g]*Department of Physics, Chungbuk National University, Cheongju 28644, South Korea. E-mail: donghyun@cbnu.ac.kr*

along different crystallographic directions, resulting in different $|\Delta S_m|$ values and reversibility between polycrystalline and a single crystal sample.[9]

Second, when one or both B-sites are occupied by nonmagnetic ions with d^0 or d^{10} configurations such as Ti^{4+} or Zn^{2+}, respectively, the super-exchange interactions between Gd^{3+} ions are small or frustrated by lattice geometry, then the system behaves like a dense lattice of almost free Gd spins down to very low temperatures. Yang *et al.*[10] reported an enormous $|\Delta S_m|$ value of ~53.5 J kg^{-1} K^{-1}, and RCP = 620.6 J kg^{-1} at a field change ΔH = 90 kOe, and ΔT_{ad} = 23.7 K for a disordered double-perovskite Gd_2ZnTiO_6. These values exceed those of the benchmark for magnetic cooling $Gd_3Ga_5O_{12}$ (GGG) in the same magnetic field change. The enhanced performance in such Zn/Ti-containing double perovskites is attributed to the minimal 3d–4f super-exchange interactions and the resulting free-spin-like response of the Gd sublattice. Comparing the two scenarios highlights the tunability of the double-perovskite motif: inclusion of magnetic 3d ion (Mn) shifts the MCE to higher temperatures set by the 3d-ordering, whereas substitution by nonmagnetic B-site ions (Zn, Ti) suppresses the cooperative 3d order and shifts the maximal MCE to lower temperatures with potentially larger per-mass magnetic entropy change due to nearly complete extraction of the Gd^{3+} entropy.[3,9–11] The FM ground state of a sol–gel synthesized Gd_2ZnMnO_6 has been proposed by both experimental study and first-principles calculations.[12] In the same work, the MCE of this polycrystalline sample has also been investigated in detail, thus providing values of $|\Delta S_m|$ = 25.2 J kg^{-1} K^{-1} and corresponding RCP = 407 J kg^{-1} for ΔH = 70 kOe. Because of the low ordering temperature (T_M) of ~6.4 K and the first-order phase transition (FOPT), Gd_2ZnMnO_6 has been suggested as a promising candidate for magnetic cooling in the liquid He temperature range. Despite the extensive investigation of Gd-based double perovskites for low-temperature magnetic refrigeration, most reported systems are either magnetically well-ordered or exhibit relatively simple PM–AFM transitions. In contrast, Gd_2MnZnO_6 introduces significant B-site disorder through partial substitution of Mn ions with nonmagnetic Zn^{2+} ions, leading to dilution of exchange pathways and enhanced magnetic complexity.

Based on these facts, it can be concluded that the rare-earth double perovskites present an opportunity: by rational B-site substitution, *i.e.* mixing magnetic and nonmagnetic ions, adjusting B-site valence and ionic size, one can tune the balance between super-exchange interactions strength and magnetic-ordering temperature, and $|\Delta S_m|$ and RCP/RC parameters. Although the MCE of a sol–gel synthesized Gd_2ZnMnO_6 sample has already been studied upon $|\Delta S_m|$ and RCP,[12] no attempts have been made so far for systematic investigation of MC behavior by means of the heat capacity (C_p) and ΔT_{ad} data. This work therefore focuses not only on the magnitude of MC response, but also on its evolution in a magnetically inhomogeneous environment. The observed broad entropy change, deviation from universal scaling behavior, and enhanced RCP highlight the role of disorder and competing interactions in tuning MC performance. Such behaviors, which are less explored compared to structurally ordered Gd-based compounds, provide valuable insight into the design of materials with broadened working temperature ranges. In this context, the present study aims to investigate the cryogenic MC properties of a Gd_2ZnMnO_6 sample fabricated *via* solid-state reactions. For practical applications, the direct measurement of ΔT_{ad}, combined with its indirect determination from C_p and magnetization (M) data, offers more comprehensive and reliable information. By comparatively analyzing the MCE using multiple approaches – including $|\Delta S_m|$, C_p, direct/indirect ΔT_{ad}, and RCP/RC – we can gain more insights into this complex material system.

2. Experimental details

In this study, a polycrystalline Gd_2ZnMnO_6 sample was synthesized *via* a conventional solid-state reaction (SSR) in air. Stoichiometric amounts of high-purity precursor oxides of Gd_2O_3, MnO_2 and ZnO (99.9%, Aldrich) were thoroughly mixed and ground, followed by calcination at 950 °C for 5 h. The calcined mixture was then reground and pre-annealed at 1250 °C for 6 h. Finally, it was ground again, pelletized under a uniaxial pressure of ~3 tons, and then sintered at 1320 °C for 12 h to ensure phase formation and improve crystalline quality. During sample synthesis, the heating and cooling rates were fixed at 3 °C min^{-1}. After sintering and cooling to room temperature, the crystalline structure of the product was characterized using an X-ray diffractometer (Bruker D8, Discover) using the radiation source of Cu-K_α with λ = 1.5406 Å. The particle morphology of the fabricated sample was examined using a field-emission scanning electron microscope (SEM, JSM-5410LV) equipped with energy-dispersive X-ray spectroscopy (EDS) working in the energy range E = 0–20 keV.

Magnetization *vs.* temperature, $M(T)$, measurements were performed using a PPMS-9 setup (Quantum Design) in a 2–300 K temperature range, with a temperature sweeping rate of 1.0 K min^{-1}. The measurements were carried out in DC magnetic fields of 1 kOe. Isothermal magnetization curves, $M(H)$, were measured in the temperature range of 2–38 K, with a δT step of 2 K and applied magnetic fields of up to 90 kOe. The temperature and ΔT_{ad} values of the sample were directly measured using a differential type-E thermocouple. This thermocouple was connected to a Keithley 2182A nanovoltmeter. The calibration of the thermocouple allowed the absolute temperature to be determined with an accuracy of at least 0.1 K, and the adiabatic temperature change with an accuracy of at least 0.02 K. It is necessary to add that the PPMS-9 instrument (for standard measurements) designed to provide high-precision data was used for the measurements is equipped with temperature sensors and a cryostat. Taking this into account, along with the fact that the addenda were measured according to standard procedures and the sample was mounted in an optimal configuration using Apiezon N (with the sample mass and geometry also being optimal for C_p measurements).

MC behavior was evaluated upon $|\Delta S_m|$, RCP and RC that were calculated by using the following expressions:[1]

$$|S_m(T,H)| = \int_0^H \left(\frac{\partial M}{\partial T}\right)_H dH, \quad (1)$$

$$RCP = |\Delta S_{max}| \times \delta T, \quad (2)$$

$$RC = \int_{T_L}^{T_H} |\Delta S_m(T)| dT. \quad (3)$$

In these expressions, δT is known as the full width at half maximum of the $|\Delta S_m(T)|$ curve that also introduces two temperature points T_H and T_L defined as cold and hot sides, respectively. The heat capacity was measured in a temperature range of 2–100 K in a zero magnetic field and fields of 10 and 40 kOe using a PPMS-9 Heat Capacity System (Quantum Design). The entropy curves $S(T, H)$ for magnetic fields $H = 0$, 10 and 40 kOe have been derived from the experimental heat capacity data $C_p(T, H)$ by integrating from 50 K to 2 K, as described in ref. 1, 3 and 13. Then, by subtracting the curve of $S(T, 0)$ from the $S(T, H)$ set, $|\Delta S_m(H, T)|$ dependencies have been obtained. The calculations of $\Delta T_{ad}(T, H)$ have been carried out in a similar manner. Thus, $|\Delta S_m(H, T)|$ and $|\Delta T_{ad}(H, T)|$ have been calculated from the heat capacity (C_p) measured in the presence (C_H) and absence (C_0) of magnetic field using the following equations:[1]

$$\Delta S_m(H,T) = \int_0^T \frac{C_H}{T} dT - \int_0^T \frac{C_0}{T} dT = S_H(T_H) - S_0(T_0) \quad (4)$$

$$\Delta T_{ad}(H, T) = T(S_H) - T(S_0) \quad (5)$$

The calculations were performed with allowance for $T_H = T_0$ (isothermal conditions) in eqn (4) and $S_H = S_0$ (adiabatic conditions) in eqn (5).

For the direct measurement of ΔT_{ad}, an experimental system described in detail by Koshkid'ko *et al.*[13] was used. Experiments were performed on the sample in magnetic fields up to 18 kOe generated by A Halbach-type magnetic field source using permanent Nd–Fe–B magnets (AMT&C Group). The temperature of the sample was measured with a differential thermocouple, and a Hall sensor placed in the sample holder was used to measure the magnetic field. A thermal screen around the sample helped to minimize heat losses to the environment.

3. Results and discussion

Fig. 1(a) shows a SEM image of our fabricated sample of Gd_2MnZnO_6. The sample appears to consist of irregular particles with random crystallographic orientations. These particles are agglomerated to form a polycrystalline ceramic material. There are also micrometer-sized interstices among the particles. The particle-size distribution histogram, as presented in the inset of Fig. 1(a), indicates an average particle size of approximately 1.9 μm. Upon analyzing EDS data for Gd_2MnZnO_6, it is observed that the spectrum shows the presence of only Gd, Mn, Zn, and O elements, as illustrated in Fig. 1(b). The average concentrations, in both mass and atomic composition percentages, were estimated from the integrated intensities of the corresponding EDS peaks. These results are tabulated and presented in the inset of Fig. 1(b). Comparing with the ideal stoichiometry (59.35% Gd, 10.37% Mn, 12.34% Zn, and 17.94% O), slight deviations are observed in experimental composition. These differences are attributed to slight nonstoichiometry and limitations of EDS measurements. In particular, a small degree of oxygen deficiency (within a few percent), as estimated from EDS data, would lead to the coexistence of Mn^{4+} and Mn^{3+} ions, based on charge balance considerations and comparisons with related double perovskites.[12] Together with Gd^{3+}, these mixed-valence states significantly influence the magnetic and MC properties of Gd_2MnZnO_6, as discussed below.

The crystal structure of the synthesized Gd_2MnZnO_6 sample was also analyzed using X-ray diffraction (XRD). Since the degree of cation ordering in double perovskite samples strongly depends on the synthesis route, structural models with B-site cation ordered and cation-disordered configurations were tested against the experimental data. As shown in Fig. 2, the XRD pattern is well described by a single orthorhombic *Pnma* disordered perovskite phase, which is a main part of the structural diagram of the perovskite compounds.[14] The refined lattice parameters were obtained as $a = 5.635(1)$ Å, $b = 7.574(1)$ Å, and $c = 5.324(1)$ Å. For the cation-ordered configurations, Rietveld refinements reveal that structural models with space groups $P2_1/n$ and $P2_1/c$, as reported in ref. 12 and 15 are able to reproduce the experimental data. However, these models do not provide a significant improvement in fit quality, despite the substantially larger number of refined parameters. Moreover, the absence of any superlattice reflections characteristic of B-

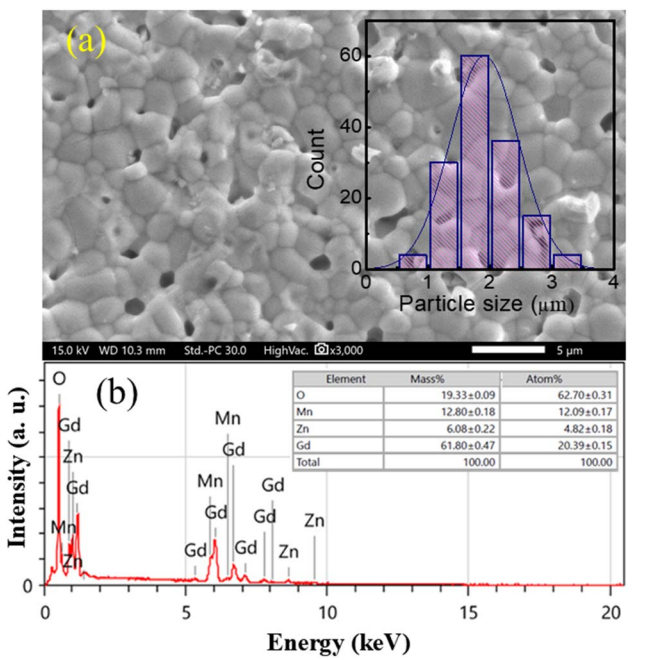

Fig. 1 (a) SEM image with a particle-size distribution histogram (the inset), and (b) EDS spectrum of Gd_2MnZnO_6, with a table showing the mass and atomic percentages of the elements Gd, Mn, Zn and O present in the sample.

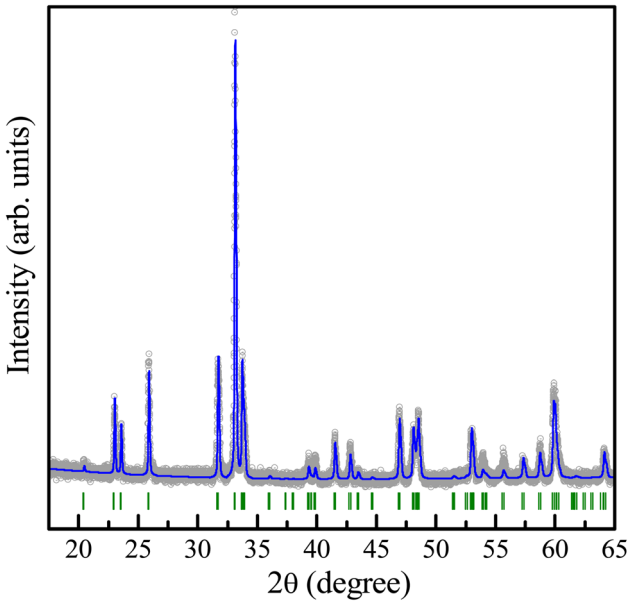

Fig. 2 XRD data for Gd_2ZnMnO_6 were analyzed using a disordered *Pnma* perovskite structural model. The open circles denote the experimental data points, and the solid line represents the fitted profile obtained through Rietveld refinement. The ticks below represent calculated positions of the nuclear peaks from the *Pnma* orthorhombic structural phase.

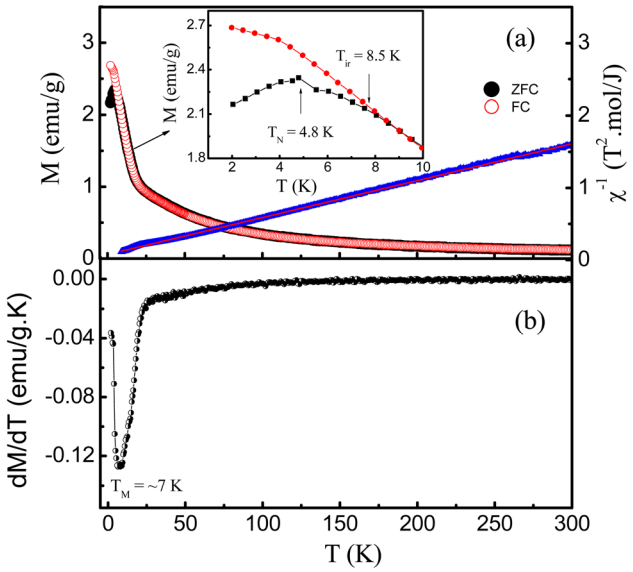

Fig. 3 (a) ZFC/FC $M(T)$ and $\chi^{-1}(T)$ curves of Gd_2MnZnO_6 at the field $H = 1$ kOe, in which the inset represents an enlarged view of experimental data at temperatures $T = 2$–10 K, indicating T_N and T_r values. (b) $dM_{ZFC}(T)/dT$ curve at the same field, which shows T_M associated with the FM–PM transition temperature ascribed to FM exchange interactions of Mn^{3+}–Mn^{4+} pairs.

site cation ordering supports the presence of the disordered *Pnma* perovskite structure of our Gd_2MnZnO_6 sample.[16]

Regarding the magnetic behavior, Gd^{3+} is known to occupy a unique position among the Ln series due to its half-filled 4f electronic configuration ($4f^7$). This leads to a highly symmetric electronic structure characterized by a pure spin ground state. According to Hund's rule, Gd^{3+} has $J = 7/2$ (the total angular momentum) because of $S = 7/2$ (the spin angular momentum), and $L = 0$ (as mentioned above), corresponding to the ground-state term $^8S_{7/2}$.[17] As a consequence, its magnetic behavior is governed purely by spin magnetism. Additionally, due to $L = 0$, Gd^{3+} ion is essentially insensitive to crystal-field effects, resulting in an effective-magnetic moment value close to the spin-only value, $\mu_{eff} = 7.94\ \mu_B$ as found experimentally in many systems.[3,18–21] This value remains nearly temperature-independent in the paramagnetic (PM) region and reflects ideal Curie–Weiss behavior.[2] Furthermore, the coexistence of Gd^{3+} ions with a transition metal ion (like Mn) introduces additional 3d–4f (or d–f) exchange interactions, which can lead to complex magnetic ordering phenomena as shown below.

Fig. 3(a) represents the temperature-dependent magnetization, $M(T)$, in the range of 2–300 K for $H = 1$ kOe (0.1 T), measured under zero-field-cooled (ZFC) and field-cooled (FC) protocols. For the $M_{ZFC}(T)$ curve, it is seen that M increases gradually with T, thus achieving a clear maximum value at 4.8 K, see the inset of Fig. 3(a). This point is assigned to the Néel temperature (T_N), which is related to the antiferromagnetic-paramagnetic (AFM–PM) phase transition driven predominantly by Gd^{3+}–Gd^{3+} (f–f) super-exchange interactions. This assignment is further supported by the corresponding λ-type anomaly observed in the heat-capacity data below. Above T_N, the rapid decrease of M becomes more gradual as T increases beyond 50 K. A similar trend is observed in the $M_{FC}(T)$ curve over the entire investigated temperature range, however, the FC curve does not exhibit a maximum at T_N, as observed in Gd_2MnCuO_6 and Li_2CoCl_4.[22,23] This behavior may be associated with field-induced alignment of magnetic moments, resulting in a suppressed AFM transition signature. We also observed the so-called irreversibility temperature, $T_{ir} = 8.5$ K, the inset of Fig. 3(a), where the ZFC and FC magnetization curves begin to diverge. This bifurcation between the ZFC and FC curves indicates the existence of AFM/FM clusters and cation disorder. These factors cause a local anisotropic field in the sample that is usually assigned to magnetic frustration and/or magnetic inhomogeneity.[24–26] Such features differ from those reported by Li *et al.*[12] for the sol–gel synthesized Gd_2MnZnO_6 sample. We assume that these differences likely originate from synthesis-dependent microstructural effects. It is well known that the sol–gel route typically yields smaller grains, higher surface-to-volume ratios, and a larger concentration of defects compared to the sample prepared by the SSR method carried out at high temperatures. Such microstructural differences in the material would influence the effective anisotropy field (H_{an}), influencing ZFC/FC splitting and field response. In our Gd_2MnZnO_6 sample, it is believed a mixed-valence state of Mn^{4+} and Mn^{3+} ions (notably, this is an inferred interpretation based on EDS-related considerations rather than a direct measurement). Besides Gd^{3+}–Gd^{3+} AFM super-exchange pairs, this can stimulate weakly FM exchange interactions of Mn^{3+}–Mn^{4+} (d–d) pairs, and AFM super-exchange interaction of $Mn^{3+,4+}$–Gd^{3+} (d–f) ones, causing competing FM and AFM behaviors. In other words, the

differences in magnetic behavior between the SSR and sol–gel samples can be due to variations in microstructure, cation distribution and oxygen stoichiometry arising from the different synthesis routes. These factors influence the ratio of Mn^{3+}/Mn^{4+}, and the strength of exchange interactions (Gd–Gd, Gd–Mn, and Mn–Mn), leading to changes in ZFC/FC splitting, transition temperatures, and the total effective magnetic moment. Additionally, the presence of the nonmagnetic Zn^{2+} ions is expected to cause a random dilution on the Mn sublattice and local structural distortions, potentially leading to frustrated cluster-like magnetic states in the sample. Further analysis of the $\chi^{-1}(T)$ curve, presented in Fig. 3(a), shows that the data follow the Curie–Weiss (CW) law in the PM region. This law is expressed as $\chi(T) = C/(T - \theta_{CW})$, in which C represents the Curie constant ($C = \mu_0 N_A {\mu_B}^2 {\mu_{eff}}^2/3k_B$), and θ_{CW} is the CW temperature. A linear fit of the $\chi^{-1}(T)$ dependences yields $C \approx 196.1$ J K mol^{-1} T^{-2}, and a negative interception of $\theta_{CW} \approx -11.3$ K with the T-axis. The negative value of θ_{CW} also indicates the predominant AFM interactions in this material system. The simultaneous existence of AFM and FM phases are ascribed to exchange interactions between Gd^{3+} and Mn^{4+}/Mn^{3+} ions, as mentioned above. If Mn^{4+} ions are dominant in the host lattice, we could calculate the theoretical magnetic moment μ_{th} of the sample according to the expression:

$$\mu_{th} = \left[2\left(\mu_{eff}^{Gd^{3+}}\right)^2 + \left(\mu_{eff}^{Mn^{4+}}\right)^2\right]^{1/2}. \quad (6)$$

with ${\mu_{eff}}^{Gd^{3+}}$ and ${\mu_{eff}}^{Mn^{4+}}$ being 7.94 μ_B and 3.87 μ_B respectively, we have obtained $\mu_{th} = 11.88$ μ_B. The experimental effective magnetic moment (μ_{exp}) of the sample has been determined *via* the equation: $\mu_{exp} = (3kC/\mu_0 N_A {\mu_B}^2)^{1/2} = 12.5$ μ_B. It should be noted that the obtained μ_{exp} value is quite close to that of sol–gel synthesized sample of 12.3 μ_B.[12] The slightly higher value of μ_{exp} could be explained with a slight oxygen deficiency which causes a change of the oxidation state of the Mn ions from (4+) to (3+). Mn^{3+} (d^4, $S = 2$) has a higher effective magnetic moment of $\mu_{eff} = 4.90$ μ_B, thus a small fraction of Mn^{3+} ions increases the total magnetic moment of the sample.

Notably, in the low temperature region from 15 to 35 K, we have also observed a broad maximum in the $\chi^{-1}(T)$ curve. At such temperatures, when the spin–spin interaction energy becomes comparable to the thermal energy (k_BT), long-range magnetic order is suppressed. As a result, the magnetic susceptibility develops a characteristic broad hump, a feature commonly seen in zigzag-chain compounds such as $SrCuTe_2O_7$.[27,28] Numerous theoretical studies of one-dimensional spin-chain models have reproduced this characteristic broad peak in the magnetic susceptibility.[28,29] Interestingly, such feature has not been observed in the sol–gel synthesized sample.[12] The diverse phenomena associated with low-dimensional magnetism have been extensively discussed elsewhere,[30,31] and the work of Landee and Turnbull provides a particularly in-depth analysis of the magnetic susceptibility in such systems.[32]

Particularly, analyzing the $dM_{ZFC}(T)/dT$ data, in addition to T_N, (see Fig. 3(b)), we have observed a clear minimum at ~7 K marked as T_M, which could be considered as the FM–PM transition, *i.e.*, the Curie temperature (T_C). In fact, the simultaneous observation of two inflection points T_N and T_M is a common feature in the Ln-transition metal systems. It is indicative of the existence of mixed magnetic states (AFM and FM) in Gd_2MnZnO_6 at low temperatures. As above, we have suggested that Gd^{3+}–Gd^{3+} (f–f) and Gd^{3+}–$Mn^{3+,4+}$ (f–d), and Mn^{3+}–Mn^{4+} (d–d) interactions are proposed to give rise to AFM ordering at the main transition temperature (T_N), and FM component associated with T_M, respectively, resulting in a two-step magnetic behavior. The first-derivative method is more sensitive in detecting T_M, which appears at a higher temperature than T_N.

When considering the $M(H)$ data measured at 2 K, we obtained a very negligible coercivity $H_c \approx 0.4$ kOe. However, at $T = 10$ K (>T_N and T_M), the $M(H)$ curve is analogous to superparamagnetic state with $H_c = 0$,[33] suggesting persisting FM/AFM clusters confined in a PM matrix. These findings are presented in Fig. 4(a and b) and in agreement with the splitting and overlapping of the $M_{ZFC}(T)$ and $M_{FC}(T)$ curves in the FM/AFM and PM states, respectively, thus proving the soft-magnetic behavior of the Gd_2MnZnO_6 double perovskite sample. Such soft-magnetic feature is highly desirable for MC applications due to reduced magnetic hysteresis losses.

A close examination of the isothermal $M(H)$ curves of Gd_2MnZnO_6 recorded between 2 and 38 K, shown in Fig. 5(a), reveals that M increases gradually as H rises from 0 to 90 kOe. Concurrently, at lower temperatures, M exhibits a nonlinear dependence on H, particularly in the low-field region. Meanwhile, with increasing T, $M(H)$ dependences become linear. These features are associated with the alignment of the

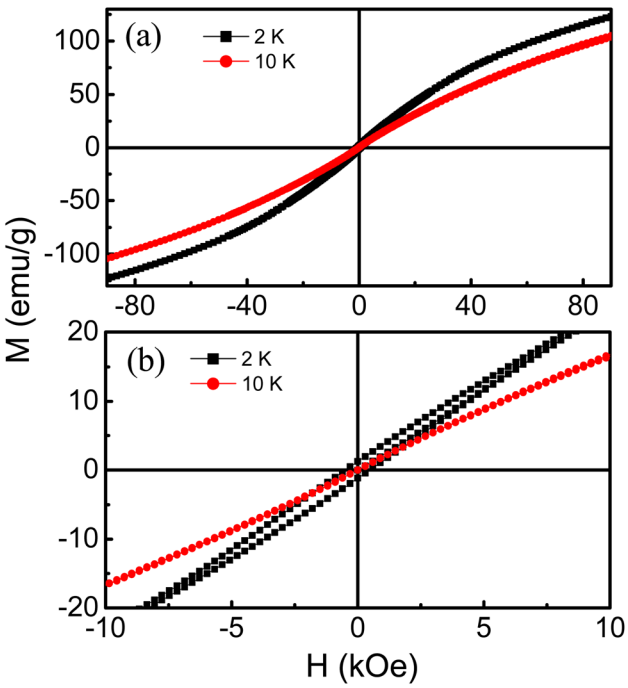

Fig. 4 (a) Full $M(H)$ hysteresis curves of Gd_2MnZnO_6 measured at temperatures $T = 2$ and 10 K, with magnetic-field changes up to 90 kOe; (b) an enlarged view of $M(H)$ data at low fields, $H < 10$ kOe.

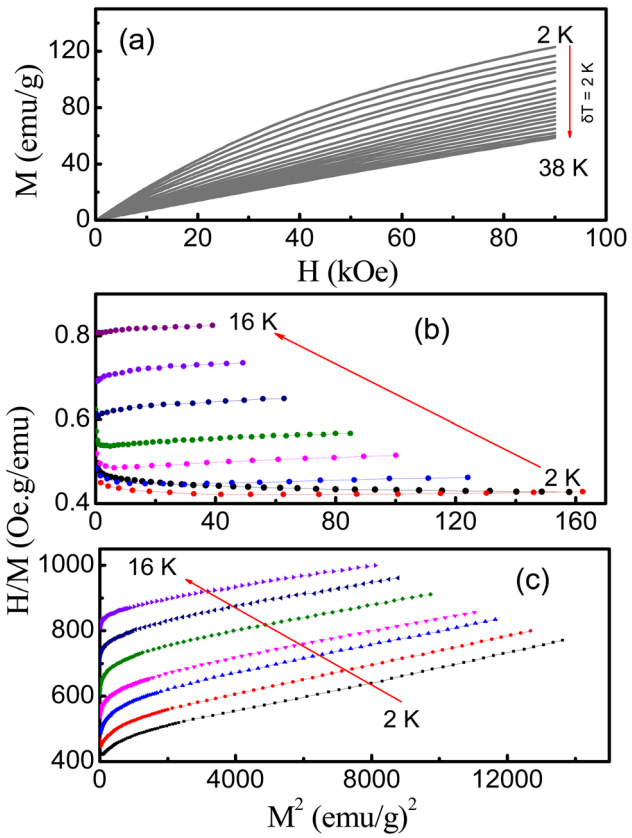

Fig. 5 (a) Representative $M(H)$ data at temperatures $T = 2$–38 K, and inverse Arrott plots of H/M *vs.* M^2 at (b) low fields and (c) high fields, in which temperature increments were fixed at 2 K.

magnetic moments to the H direction, and the transition of FM- and AFM-mixed states to the PM state under the increased thermal energy. It is noteworthy that no clear saturation of magnetization is observed even at $H = 90$ kOe. This result suggests magnetic inhomogeneity and short-range magnetic ordering in Gd_2MnZnO_6, which hinder complete spin alignment under the applied field. Furthermore, the inverse Arrott plots (M/H *vs.* M^2)[34] at $T = 2$–16 K are presented in Fig. 5(b and c). These plots provide further insights into the magnetic-phase-transition nature. Particularly, the slopes of some curves at low fields and temperatures are negative, while at high fields and temperatures they become positive (see Fig. 5(b)). These characteristics are consistent with a short-range AFM/FM state and FOPT character, suggesting magnetic inhomogeneity.

Fig. 6(a) shows the temperature dependence of $|\Delta S_m|$ for Gd_2MnZnO_6 under magnetic fields ranging from 5 to 90 kOe; in which based on measurement resolution and data spacing, the uncertainty in $|\Delta S_m|$ is estimated to be within ±5%. These data demonstrate that $|\Delta S_m|$ depends on both T and H, and consistently increases with increasing H at any given T. The strongest magnetic-entropy change ($|\Delta S_{max}|$) take place around the AFM/FM–PM transitions ($T_N = 4.8$ K, and $T_M \approx 7$ K). Under the maximum applied field of 90 kOe, $|\Delta S_{max}|$ reaches approximately 18.8 J kg^{-1} K^{-1}. The inset of Fig. 6(a) indicates that $|\Delta S_{max}(H)|$ dependences can be expressed by a power–law relationship of the type $y = a \times H^n$, with $a = 0.04$ and $n = 1.4$. In fact, n is associated with the magnetic ordering parameter derived from another parameter, N, defined as follows:[35]

$$N(T,H) = \frac{\mathrm{d}\ln|\Delta S_m(T,H)|}{\mathrm{d}\ln(H)}. \quad (7)$$

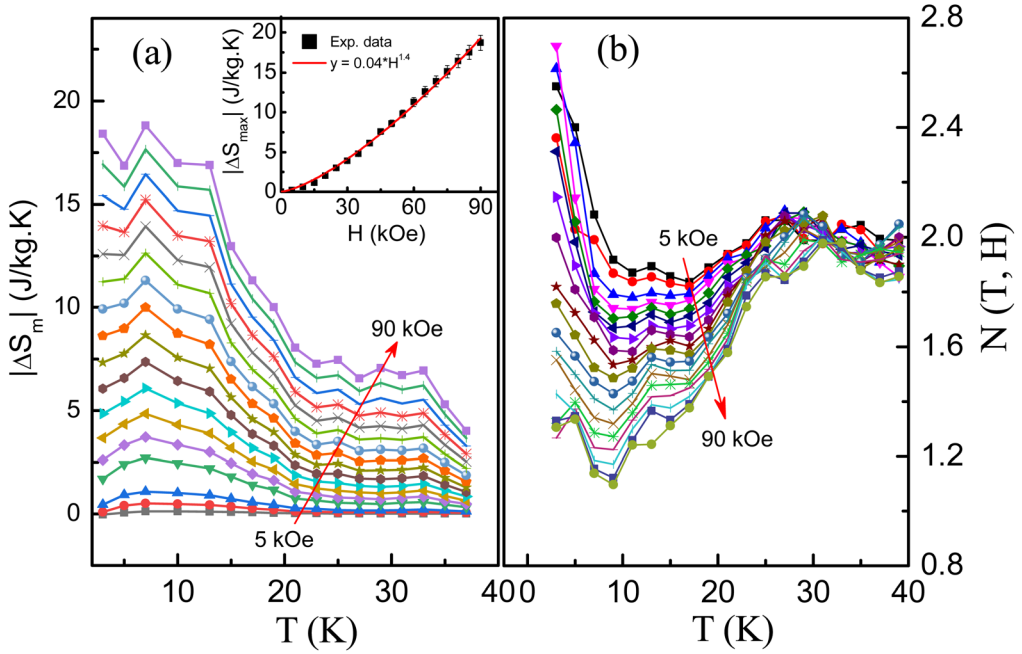

Fig. 6 (a) $|\Delta S_m(T)|$ and (b) $N(T)$ data of Gd_2MnZnO_6 at different applied fields with steps fixed at $\Delta H = 5$ kOe; the inset represents $|\Delta S_{max}(H)|$ data fitted to a power function $y = 0.04 \times H^{1.4}$ (solid curve), with error bars of ~2%.

For long-range ferromagnets, N approaches 1 and 2 in the limits $T \ll T_C$ and $T \gg T_C$, respectively, and reaches a minimum value 2/3 at $T = T_C$. Accordingly, $n = N(T_C)$, and $|\Delta S_{max}| \propto H^{2/3}$, as predicted by mean-field theory (MFT).[1,35] For our system of Gd_2MnZnO_6, though N at temperatures $T \gg T_C$ approaches 2 and is less dependent H (corresponding to the complete PM region), its value at $T < 25$ K (covering both T_N, and T_M or T_C) is different from above theorical descriptions, and strongly H-dependent. At T_M or T_C, the minimum N can change in the value range of 1.1–1.8, as shown in Fig. 6(b). Clearly, the values of n (=1.4 obtained from fitting $|\Delta S_{max}(H)|$ data to the power law) and $N(T_M/T_C)$ are notably larger than the MFT value of 2/3 (~0.67), and typical values observed for most MC materials ($n = 0.5$–0.8).[1,22,35] Such high value suggests the presence of short-range magnetic order and disorder effects in the sample, which are associated with the coexistence of f–f and f–d and d–d interactions between Gd^{3+}, Mn^{3+} and Mn^{4+} ions in Gd_2MnZnO_6. Similar large exponents have been reported in unconventional FM systems exhibiting short-range magnetic interactions.[23,36] As discussed above, this behavior may originate from the coexistence of AFM/FM interactions and the likely associated magnetic inhomogeneity.

To evaluate the feasibility of Gd_2MnZnO_6 double perovskite as a potential refrigeration material, it is necessary to consider not only $|\Delta S_m|$, but also the relative cooling power (RCP) and refrigerant capacity (RC).[1,7,35] These two quantities have been calculated according to eqn (2) and (3). Fig. 7 shows the field-dependent RCP and RC values. The results reveal a gradual increase in both parameters with increasing H up to 90 kOe. Similar to other reported systems,[3,6,8–12] the RCP values are consistently higher than the RC values. Under an applied magnetic field of 90 kOe, the RCP and RC values reach approximately 331 J kg^{-1} and 230 J kg^{-1}, respectively. According to eqn (2) and (3), achieving large values of these quantities requires a MC material exhibiting both large maximum entropy changes ($|\Delta S_{max}|$) and the broad phase-transition region. We believe that B-site disorder induced by the Zn presence modifies local exchange pathways between Gd and Mn ions by introducing competing interactions and disrupting magnetic coherence, thereby weakening the dominant magnetic ordering. Consequently, the magnetic transition becomes more diffuse (*i.e.*, broader phase-transition region), leading to an increased RCP/RC. Further analysis of RCP(H) and RC(H) dependencies indicates both these quantities obeying a power–law relationship of $y = b \times H^m$, where $b = 0.3$ and $m = 1.56$ for RCP, and $b = 0.3$ and $m = 1.48$ for RC, as illustrated in Fig. 7.

The temperature dependence of heat capacity, $C_p(T)$, of Gd_2MnZnO_6 was also investigated in the temperature range of 2–100 K under applied magnetic fields of 0, 10, and 40 kOe, as graphed in Fig. 8. Herein, C_p measurements carry an estimated uncertainty of ±2–3% due to calibration of the calorimetric system. A clear λ-type anomaly is observed at ~3.4 K, which is slightly lower than the T_N value obtained from the $M(T)$ data, corresponding to the AFM–PM phase transition. In fact, the T_N value determined from magnetization measurements is often higher than that inferred heat-capacity data. This discrepancy is commonly observed in AFM and FM systems and arises from the different sensitivities of magnetic and thermodynamic probes. While magnetization measurements directly detect the onset of long-range magnetic order, the heat capacity reflects changes in entropy and can be influenced by the development of short-range magnetic correlations above T_N, which may lead to a broadened anomaly and a peak at lower temperatures. In addition, critical fluctuations, magnetic inhomogeneity, and measurement conditions performed for two $M(T)$ and $C_p(T)$ measurements can also shift the apparent transition temperatures. It should be noticed that with increasing H, the maximum value of the $C_p(T)$ curves gradually decreases while the maximum-peak position shifts slightly towards low temperatures. Moreover, for the measurements performed in

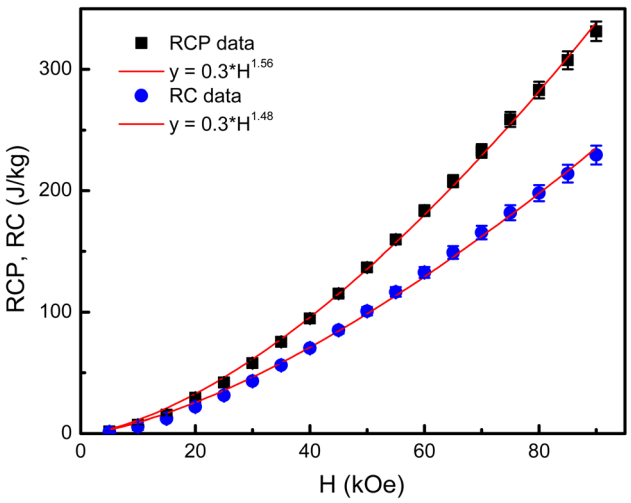

Fig. 7 H-dependent RCP and RC data of Gd_2MnZnO_6 fitted to a power function of $y = b \times H^m$, in which error bars are about 3%.

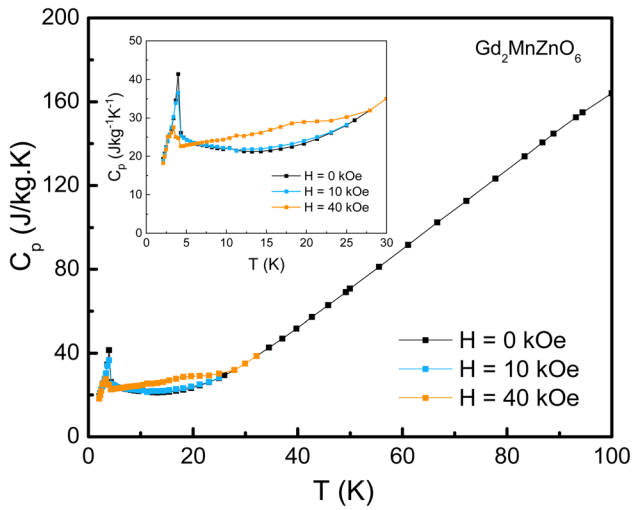

Fig. 8 Temperature dependences of C_p for Gd_2MnZnO_6 measured in zero, 10 and 40 kOe magnetic fields. The inset displays the magnified view of $C_p(T)$ data at $T < 30$ K. The λ-type anomaly associated with the AFM–PM transition slightly shift to lower temperatures as increasing H.

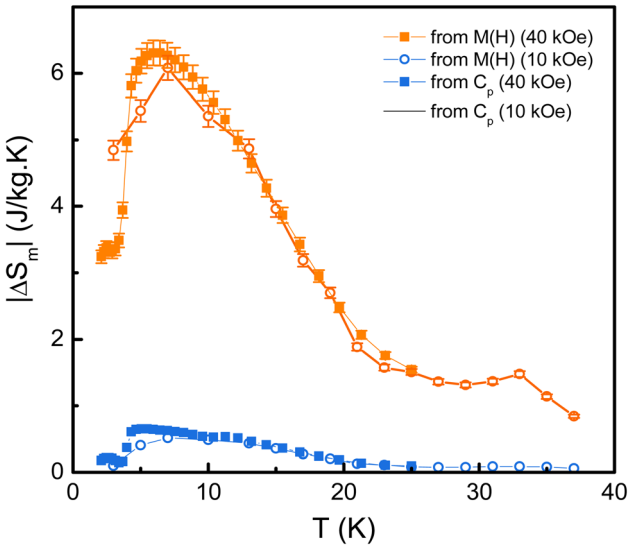

Fig. 9 T-dependent ΔS_{iso} and $|\Delta S_m|$ data (in comparison) of Gd_2MnZnO_6 calculated from $C_p(T)$ (closed symbols) and $M(H)$ measurements (open symbols) for $\Delta H = 10$ and 40 kOe, in which error bars are about 3%.

a magnetic field of 40 kOe, it can be observed that after reaching the maximum of C_p at T_N, a further increase in C_p is observed with increasing T, leading to a broad cusp in the vicinity of 18 K. This anomalous behaviour can be attributed to the Schottky contribution that arises from the crystal-field splitting of degenerate ground state energy levels of Gd^{3+}, similar to that described in other double perovskites such as Ba_2MgLnO_6 and Ba_2ZnLnO_6.[37]

Fig. 9 shows the temperature dependencies of $|\Delta S_m|$ obtained from C_p measurements and, for comparison, from M measurements in magnetic fields of 10 and 40 kOe. Both the maximum values and the shape of the of $|\Delta S_m(T)|$ curves agree well. The maximum $|\Delta S_m|$ reaches approximately 0.7 J kg^{-1} K^{-1} near 4.8 K at 10 kOe. For a magnetic field of 40 kOe, this maximum is shifted to a higher temperature, *i.e.*, 6.2 K, and reaches a value of 6.3 J kg^{-1} K^{-1}. The slight differences between the curves obtained from C_p measurements and those derived from M measurements are ascribed to the measurement accuracy of both methods. As shown by Pecharsky *et al.*,[38] the typical accuracy of the determination of $|\Delta S_m|$ from M measurements is in a range of 3–10%, and this error may become significantly higher for small $|\Delta S_m|$ values. Compared to structurally ordered Gd-based double perovskites, which often exhibit sharper magnetic transitions and higher peak entropy changes, the present system shows a reduced $|\Delta S_m|$ but broader temperature dependence. This fact emphasizes the inherent trade-off between achieving a high peak MC response and maintaining a broad operational temperature range.

For the application aspect, it is necessary to assess the adiabatic-temperature change (ΔT_{ad}) of Gd_2MnZnO_6 double perovskite under different applied fields. First, it can be indirectly derived from the $C_p(T)$ measurements for $\Delta H = 10$ and 40 kOe combining with eqn (4) and (5). These data are shown on Fig. 10(a). As expected, the H increase leads to an increase of ΔT_{ad}. For $\Delta H = 10$ and 40 kOe, the maximum adiabatic-temperature changes at $T = 12$ K are equal to ~0.3 and 2.6 K,

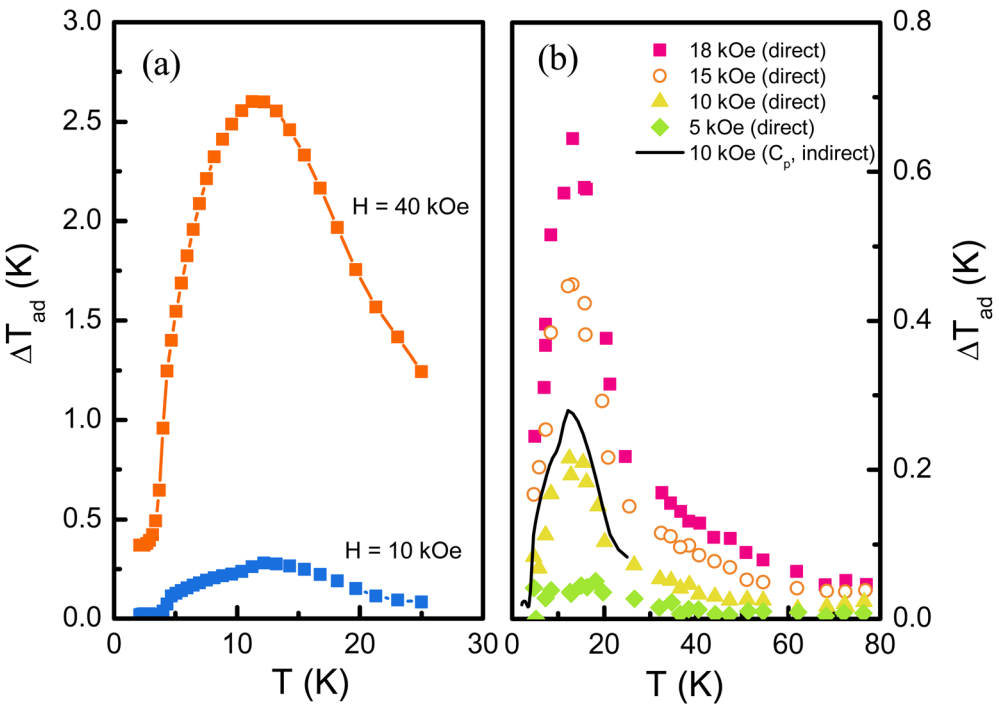

Fig. 10 (a) $\Delta T_{ad}(T)$ indirectly obtained from $C_p(T)$ data at fields 10 and 40 kOe, and (b) $\Delta T_{ad}(T)$ dependences obtained from direct measurements (symbols) at magnetic-field changes up to 18 kOe and based on $C_p(T)$ data (solid line) at 10 kOe for comparison.

Table 1 A comparison table showing MC parameters of Gd_2MnZnO_6 compared with those reported on Gd-based double perovskites at different magnetic-field variations

Compound	Synthesis method	$T_N(T_C)$ (K)	H (kOe)	$\lvert\Delta S_{max}\rvert$ (J kg^{-1} K^{-1})	ΔT_{ad} (K)	RCP/RC (J kg^{-1})	Ref.
Gd_2MnZnO_6	SSR	4.8(7)	40	6.3	2.6	95/70	This work
			90	18.8	—	331/230	
Gd_2MnZnO_6	Sol–gel	6.4	50	15.2	—	226.2/—	12
Gd_2MnCuO_6	SSR	4(8.5)	20	1.7	0.7	31/26	22
			85	16.8	—	413/303	
Gd_2MnNiO_6	SSR	130	70	35.5	10.5	—	8
Gd_2MnCoO_6	SSR	112	70	24	6.5	—	8
Gd_2MnCoO_6	Flux	112	90	25.4	8.3	—	9
Gd_2ZnTiO_6	Flux-assisted SSR	2.4	90	53.5	23.7	620.6/—	10
Gd_2FeCrO_6	Sol–gel	220	70	38.6	—	418/—	4
Gd_2MgTiO_6	Sol–gel	3.3	70	46.2	—	—/300.3	40
Gd_2FeCoO_6	Sol–gel	4.9	70	21.6	—	346/—	41

respectively. Notably, the $\Delta T_{ad}(T)$ curves around 4 K show unusual features, especially for $\Delta H = 10$ kOe, probably related to spin reorientation.[39] Additionally, we have directly measured ΔT_{ad} values of Gd_2MnZnO_6 for magnetic field changes from 5 to 18 kOe by using a differential thermocouple. It should be noticed that ΔT_{ad} obtained both directly and indirectly is subject to uncertainties related to temperature sensor calibration, thermal lag, and heat exchange. The overall uncertainty in ΔT_{ad} is estimated to be approximately ±0.1–0.2 K. The obtained results are shown in Fig. 10(b), which are also compared with $\Delta T_{ad}(T)$ obtained indirectly from $C_p(T)$ at 10 kOe. It is seen that the values of ΔT_{ad} which have been obtained by the direct measurements and by indirect method performed for 10 kOe are reasonable. For the field $\Delta H = 18$ kOe, the maximum ΔT_{ad} reaches ~0.64 K near 12 K. In Table 1, it shows the experimental values of MC parameters of Gd_2MnZnO_6 compared with those reported on Gd-based double perovskites prepared by different methods at different magnetic-field variations. It appears from Table 1 that $\lvert\Delta S_{max}\rvert$ and/or ΔT_{ad} of Gd-based compounds can change in large ranges of 1.7–54 J kg^{-1} K^{-1} and/or 0.7–23.7 K, respectively, as H changes from 20 to 90 kOe.[4,8–10,12,22,40,41] Among these, Gd_2ZnTiO_6 prepared by flux-assisted solid-state reaction exhibits largest MC parameters with $\lvert\Delta S_{max}\rvert = 53.5$ J kg^{-1} K^{-1}, $\Delta T_{ad} = 23.7$ K and RCP ≈ 621 J kg^{-1} for $H = 90$ kOe.[40] At a lower field of $H = 70$ kOe, Gd_2MnNiO_6 offers the MC-parameter values of $\lvert\Delta S_{max}\rvert = 35.5$ J kg^{-1} K^{-1} and $\Delta T_{ad} = 10.5$ K.[8] Another candidate worth mentioning is Gd_2MnCoO_6, which exhibits $\lvert\Delta S_{max}\rvert = 25.4$ J kg^{-1} K^{-1}, $\Delta T_{ad} = 8.3$ K for $H = 90$ kOe.[9] Our sample of Gd_2MnZnO_6 demonstrates moderate MC performance with $\lvert\Delta S_{max}\rvert = 6.3$ J kg^{-1} K^{-1}, $\Delta T_{ad} = 2.6$ K and RCP = 95 J kg^{-1} for $H = 40$ kOe; at a higher field of $H = 90$ kOe, it gives $\lvert\Delta S_{max}\rvert = 18.8$ J kg^{-1} K^{-1} and RCP = 331 J kg^{-1}. More details for other compounds in comparison are shown in Table 1.

4. Conclusions

We have investigated the structural, magnetic, and MC properties of the Gd_2MnZnO_6 double perovskite prepared by the SSR method. XRD analysis suggests a disordered orthorhombic *Pnma* structure of fabricated Gd_2MnZnO_6. Magnetic measurements reveal dominant AFM interactions with $T_N \approx 4.8$ K and $\theta_{CW} \approx -11.3$ K, together with signatures of competing FM contributions and short-range character arising from d–f exchange and Mn/Zn-related disorder. The compound exhibits a significant MC response, with a maximum magnetic entropy change $\lvert\Delta S_{max}\rvert = 18.8$ J kg^{-1} K^{-1} at $\Delta H = 90$ kOe, and a maximum $\Delta T_{ad} \approx 2.6$ K for $\Delta H = 40$ kOe. Direct and indirect ΔT_{ad} results are consistent with each other, and demonstrate that Gd_2MnZnO_6 is a promising candidate for cryogenic magnetic refrigeration and highlight the important role of B-site disorder in tuning magnetic interactions and MC performance in Gd-based double perovskites.

Author contributions

Dimitar N. Petrov, J. Ćwik, Yu. S. Koshkid'ko, D.-H. Kim, and T. L. Phan: conceptualization, methodology and writing; M. Babij, D. T. Khan, N. T. Dang, K. T. H. My: investigation and reviewing.

Conflicts of interest

The authors declare no competing financial interest.

Data availability

All data discussed in our manuscript could be made available on request.

Acknowledgements

Yu. S. Koshkid'ko acknowledges financial support from the National Science Center, Poland through the OPUS Program under Grant No. 2024/53/B/ST11/02445. This work was supported by Chungbuk National University NUDP program (2024) and Chungbuk National University BK21 program (2025).

References

1 A. M. Tishin and Y. I. Spichkin, *The Magnetocaloric Effect and its Applications*, CRC Press, Boca Raton, 2003, DOI: 10.1201/9781420033373.

2 J.-C. G. Bünzli, N. André, M. Elhabiri, G. Muller and C. Piguer, Trivalent lanthanide ions: versatile coordination centers with unique spectroscopic and magnetic properties, *J. Alloys Compd.*, 2000, **303–304**, 66–74, DOI: 10.1016/S0925-8388(00)00609-5.

3 E. C. Koskelo, C. Liu, P. Mukherjee, N. D. Kelly and S. E. Dutton, Free-spin dominated magnetocaloric effect in dense Gd^{3+} double perovskites, *Chem. Mater.*, 2022, **34**, 3440–3450, DOI: 10.1021/acs.chemmater.2c00261.

4 Meenakshi, S. Saini, N. Panwar, Ramovatar and S. Kumar, Giant magnetocaloric properties of Gd-based double perovskite compounds in cryogenic temperature range, *J. Magn. Magn. Mater.*, 2025, **614**, 172766, DOI: 10.1016/j.jmmm.2024.172766.

5 S. A. Ivanov, M. S. Andersson, J. Cedervall, E. Lewin, M. Sahlberg, G. V. Bazuev, P. Nordblad and R. Mathieu, Temperature-dependent structural and magnetic properties of R_2MMnO_6 double perovskites (R = Dy, Gd; M = Ni, Co), *J. Mater. Sci.: Mater. Electron.*, 2018, **29**, 18581–18592, DOI: 10.1007/s10854-018-9976-1.

6 L. Li and M. Yan, Recent progress in the development of $RE_2TMTM'O_6$ double perovskite oxides for cryogenic magnetic refrigeration, *J. Mater. Sci. Technol.*, 2023, **136**, 1–12, DOI: 10.1016/j.jmst.2022.01.041.

7 S. Vasala and M. Karppinen, $A_2B'B''O_6$ perovskites: a review, *Prog. Solid State Chem.*, 2015, **43**, 1–36, DOI: 10.1016/j.progsolidstchem.2014.08.001.

8 J. K. Murthy, K. D. Chandrasekhar, S. Mahana, D. Topwal and A. Venimadhav, Giant magnetocaloric effect in Gd_2NiMnO_6 and Gd_2CoMnO_6 ferromagnetic insulators, *J. Phys. D: Appl. Phys.*, 2015, **48**, 355001, DOI: 10.1088/0022-3727/48/35/355001.

9 J. Y. Moon, M. K. Kim, Y. J. Choi and N. Lee, Giant anisotropic magnetocaloric effect in double-perovskite Gd_2CoMnO_6 single crystals, *Sci. Rep.*, 2017, **7**, 16099, DOI: 10.1038/s41598-017-16416-z.

10 Z. Yang, J.-Y. Ge, S. Ruan, H. Cui and Y.-J. Zeng, Cryogenic magnetocaloric effect in distorted double-perovskite Gd_2ZnTiO_6, *J. Mater. Chem. C*, 2021, **9**, 6754–6759, DOI: 10.1039/D1TC01789F.

11 K. P. Shinde, E. J. Lee, A. Lee, S.-Y. Park, Y. Jo, K. Ku, J. M. Kim and J. S. Park, Structural, magnetic, and magnetocaloric properties of R_2NiMnO_6 (R= Eu, Gd, Tb), *Sci. Rep.*, 2021, **11**, 20206, DOI: 10.1038/s41598-021-99755-2.

12 L. Li, P. Xu, S. Ye, Y. Li, G. Liu, D. Huo and M. Yan, Magnetic properties and excellent cryogenic magnetocaloric performances in B-site ordered RE_2ZnMnO_6 (*RE* = Gd, Dy and Ho) perovskites, *Acta Mater.*, 2020, **194**, 354–365, DOI: 10.1016/j.actamat.2020.05.036.

13 Y. S. Koshkid'ko, J. Ćwik, T. I. Ivanova, S. A. Nikitin, M. Miller and K. Rogacki, Magnetocaloric properties of Gd in fields up to 14T, *J. Magn. Magn. Mater.*, 2017, **433**, 234–238, DOI: 10.1016/j.jmmm.2017.03.027.

14 D. P. Kozlenko, T.-L. Phan, M.-H. Phan and N.-T. Dang, Multifunctional Magnetic Oxides: Neutron Diffraction Studies, *Encyclopedia of Materials: Electronics*, 2023, vol. 1, pp. 678–693, DOI: 10.1016/B978-0-12-819728-8.00070-X.

15 R. P. Madhogaria, R. Das, E. M. Clements, V. Kalappattil, M. H. Phan, H. Srikanth, N. T. Dang, D. P. Kozlenko and N. S. Bingham, Evidence of long-range ferromagnetic order and spin frustration effects in the double perovskite La_2CoMnO_6, *Phys. Rev. B*, 2019, **99**, 104436, DOI: 10.1103/PhysRevB.99.104436.

16 J. J. P. Peters, A. M. Sanchez, D. Walker, R. Whatmore and R. Beanland, Quantitative High-Dynamic-Range Electron Diffraction of Polar Nanodomains in Pb_2ScTaO_6, *Adv. Mater.*, 2019, **31**, 1806498, DOI: 10.1002/adma.201806498.

17 C.-G. Ma, M. G. Brik, Q.-X. Li, B. Feng, Y. Tian and A. Suchocki, Energy level schemes of f^N electronic configurations for the di-, tri-, and tetravalent lanthanides and actinides in a free state, *J. Lumin.*, 2016, **170**, 369–374, DOI: 10.1016/j.jlumin.2015.07.053.

18 E. E. Oyeka and T. T. Tran, Single-ion behavior in new 2-D and 3-D gadolinium $4f^7$ materials: $CsGd(SO_4)_2$ and $Cs[Gd(H_2O)_3(SO_4)_2]\cdot H_2O$, *ACS Org. Inorg. Au*, 2022, **2**, 502–510, DOI: 10.1021/acsorginorgau.2c00031.

19 J. Goraus, P. Witas, J. Grelska, F. Calvayrac, J. Szerniewski and K. Balin, Magnetic properties of $Gd_3Cu_3Sb_4$, *J. Magn. Magn. Mater.*, 2022, **550**, 169075, DOI: 10.1016/j.jmmm.2022.169075.

20 P. P. Deen, An overview of the director state in gadolinium gallate garnet, *Front. Phys.*, 2022, **10**, 868339, DOI: 10.3389/fphy.2022.868339.

21 Y. Zhou, P. Zhou, T. Li, J. Xia, S. Wu, Y. Fu, K. Sun, Q. Zhao, Z. Li, Z. Tang, Y. Xiao, Z. Chen and H.-F. Li, Enhanced magnetocaloric effect and magnetic phase diagrams of single-crystal $GdCrO_3$, *Phys. Rev. B*, 2020, **102**, 144425, DOI: 10.1103/PhysRevB.102.144425.

22 D. N. Petrov, J. Ćwik, Y. S. Koshkid'ko, M. Babij, N. H. Nam, N. T. Dang, V. N. Thuc, D. H. Kim and T. L. Phan, Mixed magnetic-ordering states, and directly and indirectly magnetocaloric measurements in a Gd_2MnCuO_6 double perovskite, *Ceram. Int.*, 2025, **51**, 46791–46798, DOI: 10.1016/j.ceramint.2025.07.384.

23 Z. W. Riedel, Z. Jiang, M. Avdeev, A. Schleife and D. P. Shoemaker, Zero-field magnetic structure and metamagnetic phase transitions of the cobalt chain compound Li_2CoCl_4, *Phys. Rev. Mater.*, 2023, **7**, 104405, DOI: 10.1103/PhysRevMaterials.7.104405.

24 M. Svedberg, S. Majumdar, H. Huhtinen, P. Paturi and S. Granroth, Optimization of $Pr_{0.9}Ca_{0.1}MnO_3$ thin films and observation of coexisting spin-glass and ferromagnetic phases at low temperature, *J. Phys. Condens. Matter*, 2011, **23**, 386005, DOI: 10.1088/0953-8984/23/38/386005.

25 T. L. Phan, D. Grinting, S. C. Yu, N. V. Dai and N. V. Khiem, Ferromagnetism and spin- glass-like behavior in $(Nd_{0.65}Y_{0.35})_{0.7}Sr_{0.3}MnO_3$, *J. Kor. Phys. Soc.*, 2012, **61**, 1439–1443, DOI: 10.3938/jkps.61.1439.

26 D. N. H. Nam, R. Mathieu, P. Nordblad, N. V. Khiem and N. X. Phuc, Ferromagnetism and frustration in $Nd_{0.7}Sr_{0.3}MnO_3$, *Phys. Rev. B:Condens. Matter Mater. Phys.*, 2000, **62**, 8989–8995, DOI: 10.1103/PhysRevB.62.1027.

27 J. C. Bonner and M. E. Fisher, Linear magnetic chains with anisotropic coupling, *Phys. Rev.*, 1964, **135**, A640, DOI: 10.1103/PhysRev.135.A640.

28 S. Eggert, I. Affleck and M. Takahashi, Susceptibility of the spin 1/2 Heisenberg antiferromagnetic chain, *Phys. Rev. Lett.*, 1994, **73**, 332–335, DOI: 10.1103/PhysRevLett.73.332.

29 R. Feyerherm, S. Abens, D. Günther, T. Ishida, M. Meißner, M. Meschke, T. Nogami and M. Steiner, Magnetic-field induced gap and staggered susceptibility in the S=1/2 chain $[PM.Cu(NO_3)_2.(H_2O)_2]_n$ (PM = pyrimidine), *J. Phys.: Condens. Matter*, 2000, **12**, 8495–8509, DOI: 10.1088/0953-8984/12/39/312.

30 T. Giamarchi, *Quantum Physics in One Dimension*, Clarendon Press, 2003, DOI: 10.1093/acprof:oso/9780198525004.001.0001.

31 A. Vasilev, O. Volkova, E. Zvereva and M. Markina, Milestones of low-D quantum magnetism, *npj Quantum Mater.*, 2018, **3**, 1–13, DOI: 10.1038/s41535-018-0090-7.

32 C. P. Landee and M. M. Turnbull, A gentle introduction to magnetism: units, fields, theory, and experiment, *J. Coord. Chem.*, 2014, **67**, 375–439, DOI: 10.1080/00958972.2014.889294.

33 L. Bartolome, M. Imran, K. G. Lee, A. Sangalang, J. K. Ahn and D. H. Kim, Superparamagnetic γ-Fe_2O_3 nanoparticles as an easily recoverable catalyst for the chemical recycling of PET, *Green Chem.*, 2014, **16**, 279–286, DOI: 10.1039/C3GC41834K.

34 A. Arrott and J. E. Noakes, Approximate equation of state for nickel near its critical temperature, *Phys. Rev. Lett.*, 1967, **19**, 786–789, DOI: 10.1103/PhysRevLett.19.786.

35 V. Franco, J. S. Blázquez, J. J. Ipus, J. Y. Law, L. M. Moreno-Ramírez and A. Conde, Magnetocaloric effect: from materials research to refrigeration devices, *Prog. Mater. Sci.*, 2018, **93**, 112–232, DOI: 10.1016/j.pmatsci.2017.10.005.

36 K. T. H. My, A. Gayen, N. T. Dang, D. N. Petrov, J. Ćwik, T. V. Manh, T. A. Ho, D. T. Khan, D.-H. Kim, S. C. Yu and T. L. Phan, Magnetic and magnetocaloric behaviors of a perovskite/hausmannite composite, *Curr. Appl. Phys.*, 2024, **60**, 57–63, DOI: 10.1016/j.cap.2024.01.012.

37 C. A. Marjerrison, C. M. Thompson, G. Sala, D. D. Maharaj, E. Kermarrec, Y. Cai, A. M. Hallas, M. N. Wilson, T. J. S. Munsie, G. E. Granroth, R. Flacau, J. E. Greedan, B. D. Gaulin and G. M. Luke, Cubic Re^{6+} ($5d^1$) double perovskites, Ba_2MgReO_6, Ba_2ZnReO_6, and $Ba_2Y_{2/3}ReO_6$: magnetism, heat capacity, μSR, and neutron scattering studies and comparison with theory, *Inorg. Chem.*, 2016, **55**, 10701–10713, DOI: 10.1021/acs.inorgchem.6b01933.

38 V. K. Pecharsky and K. A. Gschneidner Jr, Magnetocaloric effect and magnetic refrigeration, *J. Magn. Magn. Mater.*, 1999, **200**, 44–56, DOI: 10.1016/S0304-8853(99)00397-2.

39 J. Dorantes-Dávila, R. Garibay-Alonso and G. M. Pastor, Spin-fluctuation theory of temperature-driven spin reorientations in ferromagnetic transition metal thin films, *Phys. Rev. B*, 2024, **110**, 174406, DOI: 10.1103/PhysRevB.110.174406.

40 Y. Zhang, Y. Tian, Z. Zhang, Y. Jia, B. Zhang, M. Jiang, J. Wang and Z. Ren, Magnetic properties and giant cryogenic magnetocaloric effect in B-site ordered antiferromagnetic Gd_2MgTiO_6 double perovskite oxide, *Acta Mater.*, 2022, **226**, 117669, DOI: 10.1016/j.actamat.2022.117669.

41 Z. Dong and S. Yin, Structural, magnetic and magnetocaloric properties in perovskite RE_2FeCoO_6 (RE = Er and Gd) compounds, *Ceram. Int.*, 2020, **46**, 1099–1103, DOI: 10.1016/j.ceramint.2019.09.077.